



Numerical simulation of modified Trombe-Michel Walls with exergy and energy analysis



Sandra Corasaniti, Luca Manni, Flavia Russo, Fabio Gori*

Department of Industrial Engineering, University of Rome "Tor Vergata", Via del Politecnico 1, 00133 Rome, Italy

ARTICLE INFO

Keywords:

Modified Trombe-Michel Wall
Sharp edges
Rounded edges
Guided flow
Exergy and energy analysis

ABSTRACT

Numerical simulations of three configurations of a modified Trombe-Michel Wall (TMW) are carried out and the numerical results are employed to carry on the energy and exergy analyses. The three configurations of the modified Trombe-Michel Wall (TMW) investigated are with sharp edges, with rounded edges and with the guided flow. For each configuration and glaze spacing, spanning from 0.1 m up to 0.5 m, the velocity and the mean air temperature in the channel, the heat flux, the exergy gain and the conductive heat transfer through the massive wall are evaluated numerically. The comparison among the three configurations shows that the guided flow presents the highest energy and exergy efficiency.

1. Introduction

The global energy consumption for the building sector in the European Union is nowadays around 40%, with about two-thirds due to heating, ventilating and air conditioning (HVAC). A Directive of the European Union suggested in 2010 that all EU members should approve energy policies to promote very low energy consumption “passive” buildings, [1].

The use of Double Skin Facades (DSF) attracted the interest of the researchers because of their capability to store solar energy and to release it gradually by keeping the internal temperature within the comfort range. One of the oldest and cheapest ways to realize a DSF is the Trombe-Michel Wall (TMW), based on a special type of envelope, where the second layer is a transparent glazing (made of glass or of a high transparent polymer). The aim of the TMW is to exploit solar energy, to storage it during peak-use periods using the heat capacity of the building materials, and to supply energy. In a typical TMW configuration, solar energy is absorbed on the black-painted south-facing wall, which increases its temperature until natural convection occurs. The density changes drive the flow through the narrow gap between the massive wall and the glazing, and the chimney effect causes the cooler air from the room to be drawn in through the bottom vent. Even if a correct configuration of the wall provides a natural convection transport mechanism, the installation of a mechanical device, such as a blower, allows the air circulation to achieve a better control of the heat transfer. Moreover, the incident energy is also transferred to the internal conditioned space by conduction through the storage wall, with a delay function of the thermal properties of the wall material and its

thickness.

Analytical techniques were developed in [2–3] to predict the hydrodynamic characteristics of a TMW, and compared with the numerical results of the same authors. The effect of the variable properties on natural convection inside an asymmetrically heated vertical channel was investigated in [4] with the numerical simulation of the recirculation patterns. It was found that the recirculation zone decreases due to the variable properties, while the mass flow rate increases and the Nusselt number is influenced until reversal flow exists.

As far as the turbulence modeling in natural convection problems is concerned, low Reynolds $k-\epsilon$ model was used in [5], founding that the turbulence intensity at the channel inlet influences the location of the transition point from laminar to turbulent flow. The influence of the channel width of a TMW on the air flow rate, as far as pressure losses are concerned, was investigated in [6]. The study pointed out that the increase of the channel width, over a certain value, does not lead to a greater air flow rate because losses are mainly located in the orifices. The same conclusion was found on the mass flow rate, which increases until a maximum value and then decreases, [7].

The shape and arrangement of the absorbing surfaces of the collectors to provide greater heat transfer, suitable for the passive heat transfer augmentation techniques, were investigated experimentally in [8]. The performance of air solar collectors, with staggered absorber sheets and attached fins on absorber surface, were tested. The efficiency of the solar collector increases approximately of 10% to 30% in comparison with the conventional solar collector. Even though scientific literature exhibits a certain shortage of experimental data, some transient results are reported in [9]. A numerical model for a composite

* Corresponding author.

E-mail address: gori@uniroma2.it (F. Gori).

TMW was validated experimentally in [10], showing that the composite TMW has better energy performances than the classic one in cold and/or cloudy weather.

Several researchers focused their studies on smaller and cheaper modifications, such as the shape of the channel. Plates with optimized spacing in the channel can maximize the induced mass-flow rate, within C-shaped channels with a TMW configuration, by assuming isothermal walls [11]. Smaller channel depth presents significant friction losses, while larger channel depth increases the heat losses in solar air heaters [12]. A non-symmetrical heated vertical plane, representative of several geometries, from chimney to Trombe wall, was investigated experimentally in [13]. The appearance of the flow regime is dependent on the Rayleigh number, since, at high values, the boundary layer is always present and a reverse flow is close to the unheated wall.

The 3D analysis is avoidable and the variations of the thermal properties with the temperature are negligible, [14]. The RNG version of the $k - \varepsilon$ turbulence model was preferred, rather than the $k - \omega$ family of models, because of the better accuracy for the heat transfer prediction, even though only few experimental data are available to validate turbulence models. Numerical 2D simulations of the TMW performance and indoor air environment were investigated in unsteady state condition for a room located in Iran [15]. The results showed that a Trombe wall, made of paraffin wax, can keep the room warmer for about 9 h.

The energy efficiency of finned double-pass solar collectors was evaluated in [16]. Some turbulence models were considered in a 3D problem, [17], where solar load was taken into account. The results indicated that the low Reynolds shear stress model is a better turbulent model, even though it requires the solution of the whole Reynolds stress tensor. As far as the performance is concerned, the exergy analysis can play an important role in the investigation. Exergy performance of plate solar collectors was investigated in [18]. The optimum values of the collector inlet temperature, mass flow rate, absorber plate area, and fluid outlet temperature were obtained for the maximum exergy inflow from the system.

The thermal behavior of a new TMW configuration, employed in the Mediterranean region, was investigated in [19]. The comparison of the results with a classic TMW showed that thermal fins contribute to the increase of the internal room temperature rise and the decrease of the external temperature, allowing a significant improvement in the thermal efficiency. A TMW with venetian blind was studied to predict its thermal behavior [20]. The numerical results demonstrated that the average temperature of the air in the room was about 5 K higher than in a classic TMW. The penetration of the natural convection in vertical parallel plates with an asymmetrically heated wall was investigated numerically in [21], with the flow reversal caused by buoyancy.

The present work is motivated by the shortage of exergy analysis of the Trombe-Michel Wall (TMW) in the literature. The principal aim is to perform an exergy analysis, which requires the numerical investigation of the thermal and fluid dynamics characteristics of the TMW. Three new configurations are investigated in order to reduce losses, increase the mass flow rate and the heat transfer, for several channel widths and a given heat flow on the irradiated surface.

Nomenclature

Latin symbols

c_p	specific heat of air, J/(kg K)
\dot{E}_x	exergy, W/m
L	glaze spacing, m
\dot{m}	mass flow rate, kg/(s m)
p	pressure, Pa
\dot{Q}	heat power, W/m
T	temperature, K
u	velocity, m/s
$u^* = \sqrt{\frac{\tau_w}{\rho}}$	friction velocity, m/s

y	distance from wall, m
$y^+ = \frac{u^* y}{\nu}$	dimensionless wall distance

Greek symbols

δ_{ij}	Kronecker delta
Δ	difference
ν	kinematic viscosity, m ² /s
ρ	density, kg/m ³
τ	shear stress or Carnot Factor, N/m ²

Subscripts

am	ambient
d	destroyed
des	desired
inl	inlet
m	mean
out	outlet
p	constant pressure
rad	radiation
s	sun
t	turbulent
w	wall

2. Trombe-Michel Wall configurations

Fig. 1 reports the three configurations of the TMW investigated. Fig. 1a is the basic one, named “sharp edges”. Fig. 1b is the configuration named “rounded edges” on the inlet and the outlet vents. Fig. 1c is the configuration named “guided flow”, which is derived from the second one by adding the guide vanes on the bottom of the channel to limit the flow detachment from the heated wall.

The first configuration is the classic TMW; a vertical channel between the irradiated surface of the massive wall and the glaze covering, usually made of transparent material, as glass or polycarbonate. Most of the solar energy is out of the visible band, and the choice of the material could strongly affect the overall performance of the system. The configuration with “sharp edges” has two orifices of the same height. Losses of efficiency are mostly due to the shape of the orifices and their dimensions. Since one purpose of this study is to reduce losses, the inlet and outlet vents are modified with the configurations with “rounded edges” and “guided flow”. The “guided flow” configuration should avoid the flow detachment with the use of four blades downwind the bottom vent. The heat transfer over the irradiated vertical surface is assumed as an average value over the whole day. The heat transfer is the same for all the geometries, because the aim of the present work is to highlight the effect of the channel depth and the shape of the orifices.

3. Numerical analysis

3.1. Computational modeling

The numerical simulations are carried out with several spacing between the cover glazing and the irradiated wall. For each of the three configurations, the interspace thickness (L) is increased from 0.10 m to 0.50 m, with a step of 0.02 m. The total height is 3 m, the wall thickness 0.4 m, as the length of the inlet and outlet vents. The boundary conditions at the orifices are selected as pressure outlet, with inflow temperature of 20 °C on the lower vent. A temperature of 0 °C is imposed on the cover glazing, in order to overestimate the thermal losses of the whole heating system. The irradiated wall heat flux is assumed as 300 W/m². Top and bottom sides of the massive wall allow the heat transfer with the airflow. The other side of the massive wall has a heat transfer coefficient of 5 W/m² K, with 20 °C of room temperature. The radiated wall has a constant heat generation rate, since the aim of this

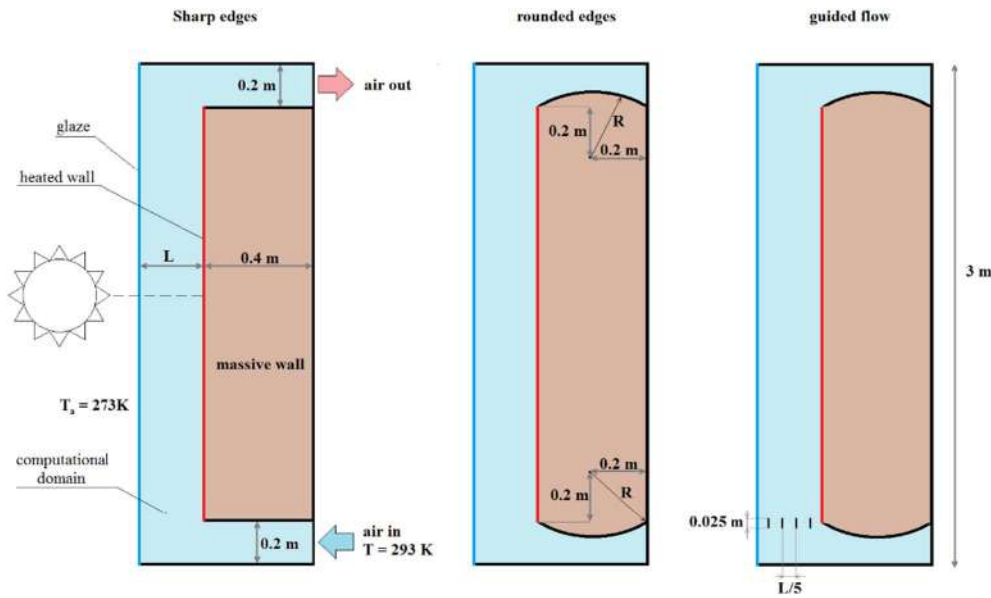


Fig. 1. The three configurations of the TMW.

work is to evaluate the effect of the shape of the orifices. Even though a fixed heat flux represents an approximate solution, because of the transient nature of the solar radiation, it is easier to estimate the radiated heat flux, rather than the wall film equilibrium temperature reached during the irradiation period, as done in [22].

The meshes of the computational domain, shown in Fig. 2, are structured to allow a better accuracy, but only the bottom part is represented. The dimensionless distance to the wall is equal to $y^+ = 1$, which allows to fully solve the boundary layer. Also the massive wall is meshed. The grid independence shows that the use of a thicker mesh increases only the run time. In the fluid domain, continuity, momentum and energy equations of air are solved, while in the solid domain only the energy equation.

3.1.1. Governing equations

The governing equations of the present work are the incompressible, Reynolds-Averaged Navier-Stokes (RANS) equations, or, the mass conservation, the two momentum and the energy conservation equations. The RANS equations are obtained by ensemble-averaging the Navier-Stokes equations and dropping the average of the fluctuating term,

$$\frac{\partial u_i}{\partial x_i} = 0 \quad (1)$$

$$\frac{\partial}{\partial x_j} (u_i u_j) = -\frac{\partial p}{\partial x_i} + \frac{\partial}{\partial x_j} \left[\nu \left(\frac{\partial u_i}{\partial x_j} + \frac{\partial u_j}{\partial x_i} - \frac{2}{3} \delta_{ij} \frac{\partial u_l}{\partial x_l} \right) \right] + \frac{\partial}{\partial x_j} (-\overline{u'_i u'_j}) \quad (2)$$

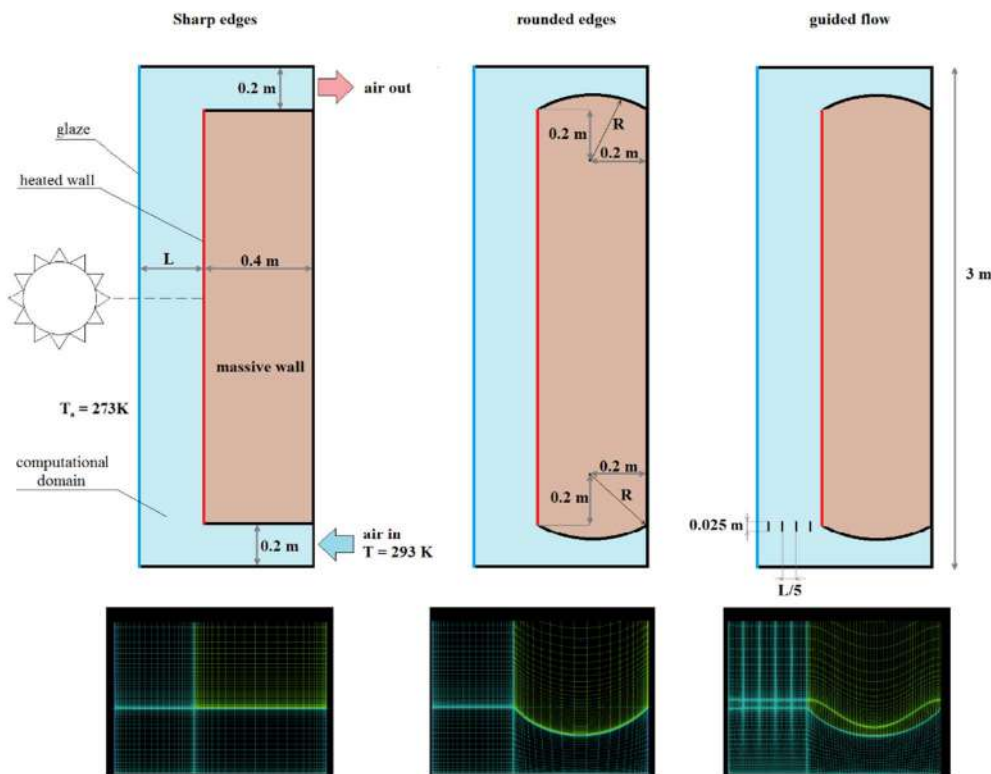


Fig. 2. Meshes of the computational domains.

The turbulence effects on the mean motion cannot be computed from the averaged equations and need to be computed in another way. A widely used method is to employ the Boussinesq hypothesis, which requires a relatively low computational cost, stating a correlation between the mean velocity gradient and the Reynolds stress tensor components

$$-\overline{u_i' u_j'} = \nu_t \left(\frac{\partial u_i}{\partial x_j} + \frac{\partial u_j}{\partial x_i} \right) - \frac{2}{3} \left(k + \nu_t \frac{\partial u_k}{\partial x_k} \right) \delta_{ij} \quad (3)$$

This hypothesis requires the assumption of the turbulent viscosity ν_t to be an isotropic scalar field, whose losses in accuracy are usually considered relatively small in comparison with the reduction in computational time. The eddy viscosity models (EVM) use this approach, but, in order to increase accuracy in highly non-isotropic flows, each term of the tensor should be modeled separately using a stress-transport model. As far as the buoyancy effects are concerned, an ideal gas model for the density is not required, because the range of temperature variation is relatively small. Boussinesq model can take into account the buoyancy effect. The temperature does not directly affect the density of the fluid through the equation of state, but appears only in the buoyancy force, as a source term in the momentum equation. This assumption allows using incompressible equations even though the density variations are actually involved in the buoyancy driven flows. SIMPLE algorithm is employed for the pressure – velocity coupling. Second order schemes are used for all the solutions.

3.2. Validation of computational methods

The test case is a tall cavity, investigated experimentally in [23], with the same dimensions of $0.076 \times 2.18 \text{ m}^2$. Thermal boundary conditions are approximately close to constant heat flux, while the shear stress varies and also changes sign close to the wall, requiring the full boundary layer solution. In order to choose the most suitable turbulence model, several of them are tested: the SST $k - \omega$, [24], the RNG version of the $k - \epsilon$ model, [25], the $\nu^2 - f$ model, [26], and the low-Re stress- ω model, based on the ω equations and LRR model [27]. The SST and the RNG model represent the classical eddy viscosity approach, which assumes turbulence isotropy, but, while the SST model achieves the computation of the viscous sub layer, the RNG model requires the use of wall functions, so-called Enhanced Wall Treatment, EWT. The EWT consists of a two-layer model: the viscosity-affected near the wall region is completely resolved all the way to the viscous sublayer by using the one-equation model of [28], while the fully turbulent outer region is modeled with the RNG $k - \epsilon$ turbulence model. A wall-distance-based turbulent Reynolds number is defined to evaluate the ending point of the laminar region and consequently the beginning of the turbulent one. The computation of the turbulent viscosity takes place using a blending function, which produces a continuous variation between the two regions. On the other hand, the $\nu^2 - f$ approach makes the distinction between the turbulent fluctuations, normal to the streamlines, and the others. Since it works well in recirculating bubbles, it is supposed to predict in a more detailed way the transition and the detachment point, rather than the previous 2-equations models. Because of its elliptic under relaxation approach, it does not require the wall function. Lastly, the low-Re stress ω model solves the transport equation for each term of the Reynolds stress tensor, hence a more accurate solution is expected.

The simulations of the tall cavity produce useful information on the mesh density. The height of the first cell has a great influence on the accuracy of the turbulent flow predictions, and a method to establish a correct mesh spacing near the wall is to evaluate the non-dimensional wall distance, y^+ . For models which solve the boundary layer, the mesh needs a first cell thickness equal to $y^+ \sim 1$. To this aim, the first node spacing of $2 \cdot 10^{-4} \text{ m}$ and a grow rate of 1.1 are set, as shown by the mesh close-up of Fig. 3. As far as the other nodes positioning is

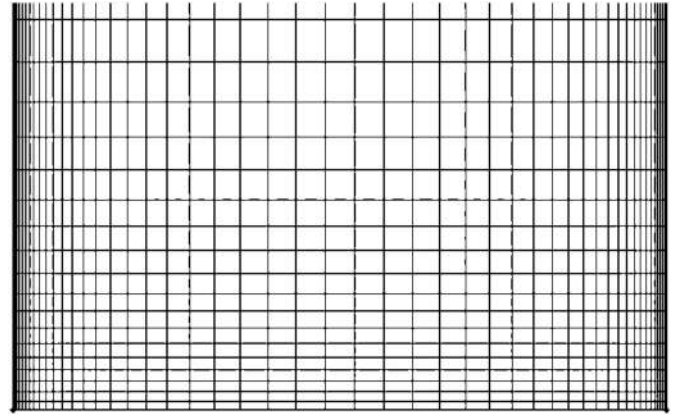


Fig. 3. Close-up of the tall cavity test case mesh.

concerned, the most suitable value for Δx_{MAX}^+ (i.e. the ratio between the maximum cell spacing and the channel width) is approximately $5 \cdot 10^{-2}$, yielding a 50-nodes mesh along the width of the cavity. In the y direction, mesh is fine enough to allow the solver to predict correctly the vertical components of the gradients, 300 nodes, with a 0.001 m wall spacing, represents a good compromise, furthermore, it allows to keep cells aspect ratio below 50, which is considered small enough to limit the numerical diffusion.

As far as turbulence modeling is concerned, the velocity field is evaluated along the middle height line of the cavity, in order to compare the models tested with the experimental values. The Rayleigh number in the present work varies from $5.26 \cdot 10^6$ to $6.57 \cdot 10^8$ for the width. Computed and measured velocity profiles are divided by the corresponding maximum value along the $y/H = 0.5$ line. Good agreement between SST $k - \omega$, RSM – stress ω turbulence models and the experimental data is found, as shown by Fig. 4. It should be noted that the enhanced wall treatment, applied to the RNG $k - \epsilon$ model, produces results very similar to the more complex $\nu^2 - f$ model, probably because of the simplicity of the test case.

4. Results and discussion

4.1. Energy analysis

The convective heat transfer and the mass flow rate are evaluated in order to evaluate the energy performance. The air temperature on the inlet is assumed equal to 20°C and the convective heat transfer is

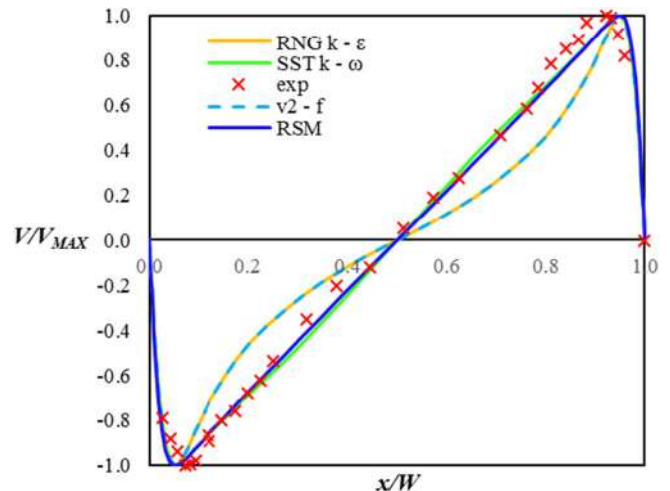


Fig. 4. Comparison between velocity predictions, with different turbulent models, and the experiments [23] for the tall cavity test case.

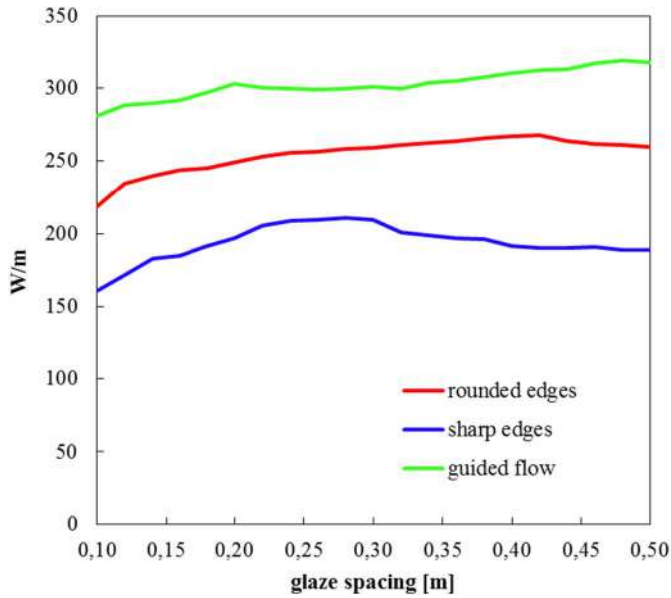


Fig. 5. Convective heat transfer per unit depth of the wall for the three configurations.

$$\dot{Q} = \dot{m}c_p(\bar{T}_{Outlet} - \bar{T}_{Inlet}) \quad (4)$$

The numerical results of the convective heat transfer are reported in Fig. 5, which shows the heat transfer per unit depth over the channel width for the three configurations. In the “sharp edges” configuration the convective heat transfer presents a maximum in the range of the glass spacing 0.25–0.30 m. This behavior is due to the presence of two phenomena. Slower air is flowing in the cavity, and, consequently, a longer time is required to the air to flow over the heated wall, and, at the same time, the convective heat transfer increases with the mean velocity. A greater convective heat transfer increases the heat losses, because of the glass temperature, and a maximum is expected. A narrower cavity produces a smaller airflow, so more heat is transferred by conduction through the wall. On the other hand, a wider cavity leads to a greater heat transfer through the glass covering. The configuration with “rounded edges” presents a maximum at a wider glass spacing, 0.42 m, and the “guided flow” one at 0.48 m, performing better, as far as the convective heat transfer is concerned.

As far as the mass flow rate is concerned, the numerical results are reported in Fig. 6, which presents the mass flow rate per unit depth of the channel width. The “guided flow” configuration reduces the early flow detachment at the bottom of the heated wall, producing a greater heating and leading to a greater buoyancy effect. The present numerical results show a greater mass flow rate for the “rounded edges” configuration than the “guided flow”, which exhibits comparable values to the “sharp edges” one.

The previous conclusions can be understood by the observation of the path-lines reported in Fig. 7, shown for the three configurations with three values of the channel width. It is evidenced the formation of a large vortex that moves from the corner, at the base of the cover glazing, toward the middle of the channel. The dimension of this vortex increases with the width of the channel, and, for the largest one, it is possible to see the foci of the two counter rotating vortices, which can be avoided with the introduction of the vanes, but only partially. The development of the vortex structures is present regardless the presence of the blades, which are able to improve the air flow only for narrow channel. The three images on the left of Fig. 7 show that the “sharp edges” configuration leads to a large flow detachment, the “rounded edges” geometry reduces the dimension of the separation bubble, while the “guided flow” one prevents the separation. It could be concluded that the blades effectiveness in the “guided flow” strongly depends on the channel depth.

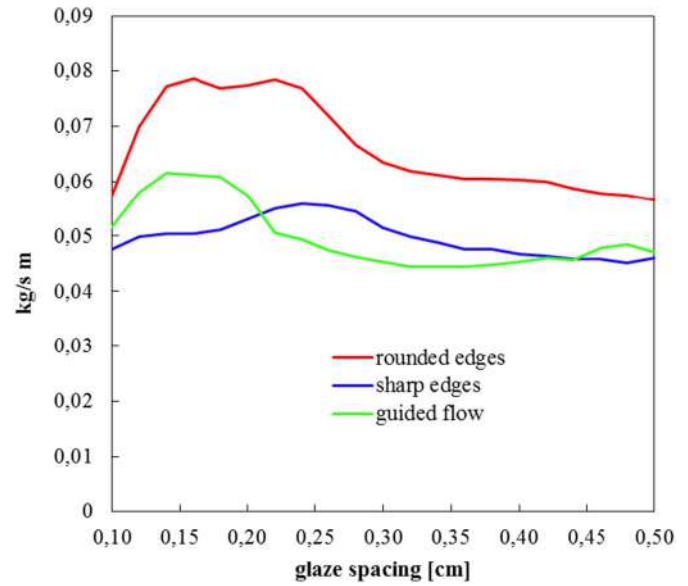


Fig. 6. Mass flow rate per unit depth of the wall for the three configurations.

Fig. 8 shows the conductive heat transfer through the wall. The “guided flow” configuration presents the smaller conductive heat transfer, because the heat transfer into the volume, in real time, is greater.

Fig. 9 shows the velocity flow fields along the channel for the three configurations. The velocity maps enlighten the locations of the losses. The difference between the sharp edges configuration and the other two is at the top of the outlet vent. A large flow separation bubble rises from the top corner of the heated wall toward the outlet, diminishing the effective sectional area of the outlet duct. As far as the other two configurations are concerned, this separation is hindered by the smooth shape of the channel, but is still present. On the other hand, in the bottom part, a comparison among the separation bubbles can help to understand the results shown in Fig. 6. While the dimension of the separated flow area is reduced by the vanes in the “guided flow” configuration, they introduce local losses that have an overall negative effect. The boundary layer, due to the air cooling of the covering glaze, forces the fluid to fill just one fraction of the channel.

The temperature fields are reported in Fig. 10 for the three configurations. Even though the differences among the three configurations are not severe, one point deserves some considerations. The recirculating zone at the bottom of the heated wall is the main difference also in the temperature field. In the recirculating bubble the velocity is smaller as well as the heat transfer coefficient. Largest is the bubble and smaller is the total surface available for the heat transfer from the wall to the air. Then, the heat transfer in the “guided flow” configuration is greater than the other two. The other effect, due to the presence of the vanes, is to fill the near wall zone of colder air that can transfer more heat from the wall.

The thermal efficiency of each configuration is defined as

$$\eta = \frac{\dot{m}c_p(\bar{T}_{Outlet} - \bar{T}_{Inlet})}{I_{rad}} \quad (5)$$

Fig. 11 reports the values of the thermal efficiency per unit depth of the wall for the three configurations. The “guided flow” configuration has the greatest value, which increases with the glaze spacing because the heat transfer is the highest, as shown by Fig. 5. The previously mentioned effect of the vanes is also the reason for the highest thermal efficiency, shown by Fig. 11. In the other two configurations a maximum is present, which is more evident for the “sharp edges” configuration.

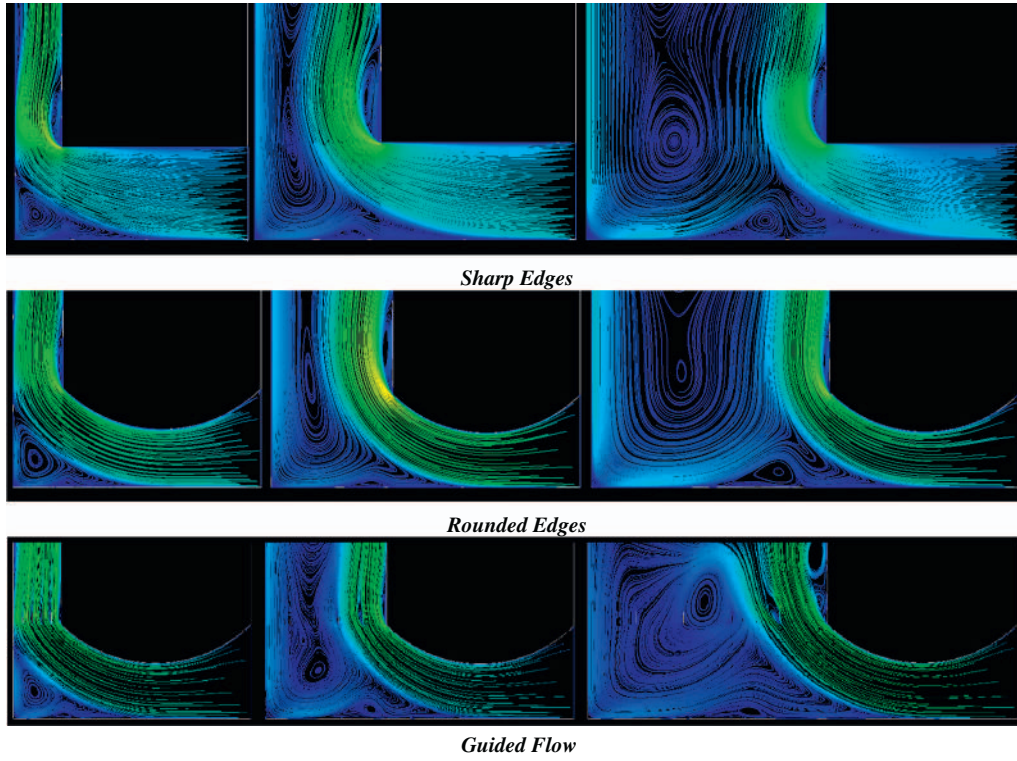


Fig. 7. Path-lines in the three configurations with three channel widths.

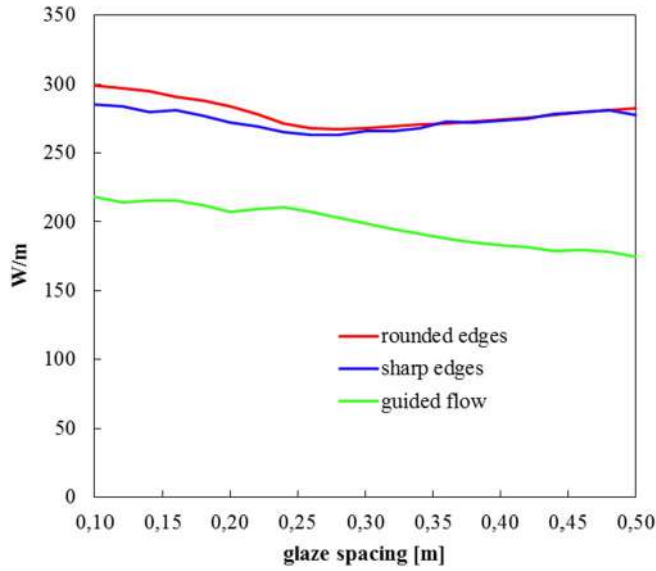


Fig. 8. Conductive heat transfer per unit depth of the wall for the three configurations.

5. Exergy analysis

The exergy balance of the problem is

$$\dot{E}x_{rad} + \sum \dot{E}x_{inl} - \sum \dot{E}x_{out} - \sum \dot{E}x_{loss} - \sum \dot{E}x_d = 0 \quad (6)$$

where $\dot{E}x_{rad}$ is the exergy of the solar radiation

$$\dot{E}x_{rad} = I \cdot \tau_s = I \cdot \left[1 - \frac{4}{3} \cdot \frac{T_{am}}{T_s} + \frac{1}{3} \cdot \left(\frac{T_{am}}{T_s} \right)^4 \right] \quad (7)$$

$\dot{E}x_{inl}$ the inlet exergy flow, $\dot{E}x_{out}$ the outlet exergy flow, $\dot{E}x_{loss}$ the lost exergy, $\dot{E}x_d$ the total destroyed exergy due to the irreversibilities. The exergy gained, $\dot{E}x_{gain}$, is given by the exergy balance in the control volume

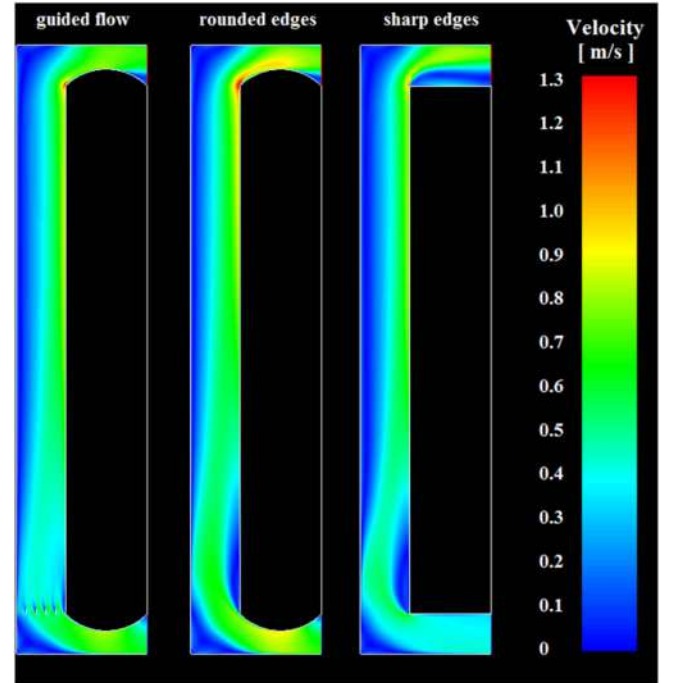


Fig. 9. Velocity flow fields for the three configurations.

$$\dot{E}x_{gain} = \dot{E}x_{out} - \dot{E}x_{inl} = \dot{m} \cdot c_p \cdot \left(T_{out} - T_{inl} - T_{am} \cdot \ln \frac{T_{out}}{T_{inl}} \right) - \frac{\dot{m}}{\rho} \cdot \Delta p \cdot \frac{T_{am}}{T_m} \quad (8)$$

where T_{am} is the ambient temperature, T_s the sun temperature and Δp the pressure drop.

The exergy efficiency is the ratio between the gained exergy and the exergy of solar radiation.

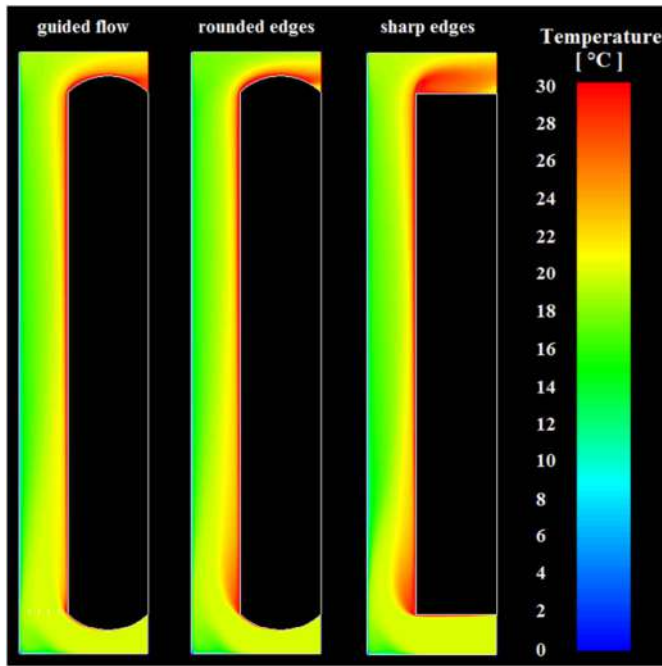


Fig. 10. Temperature fields for the three configurations.

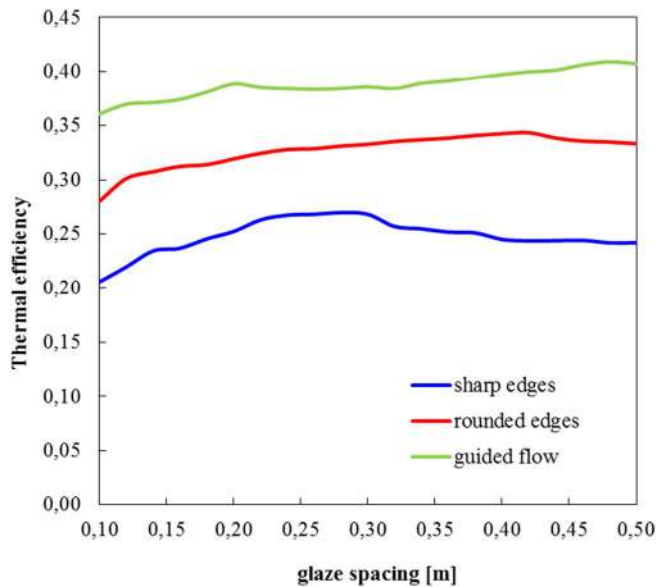


Fig. 11. Thermal efficiency per unit depth of the wall for the three configurations.

$$\eta_{ex} = \frac{\dot{E}x_{gain}}{\dot{E}x_{rad}} \quad (9)$$

The exergy analysis requires the thermal and fluid-dynamic analysis of the problem. Fig. 12 shows the exergy gain, $\dot{E}x_{gain}$, which is higher for the “guided flow” configuration and is increasing with the glaze spacing. In the other two configurations the exergy gain, $\dot{E}x_{gain}$, is smaller and presents a maximum.

The exergy efficiency is reported in Fig. 13. The “guided flow” configuration presents the greatest values, with the exergy efficiency increasing with the glaze spacing. In the other two configurations a maximum is present. The absolute values of the exergy efficiency are small because of the small temperatures involved.

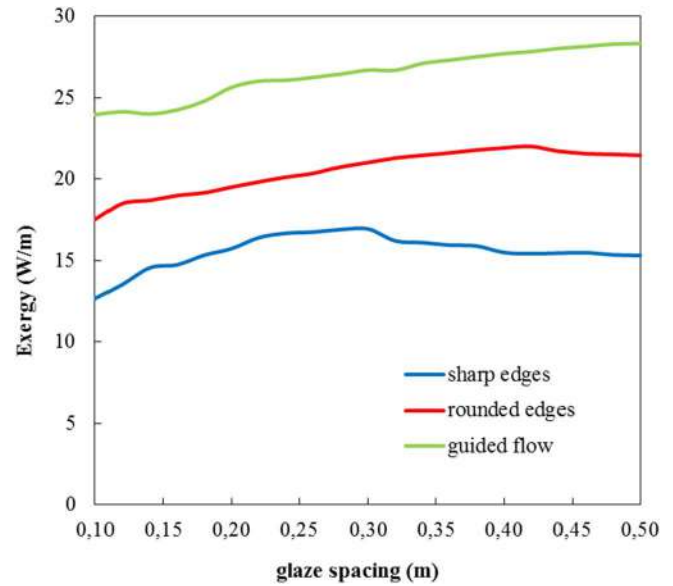


Fig. 12. Exergy gain per unit depth of the wall for the three configurations.

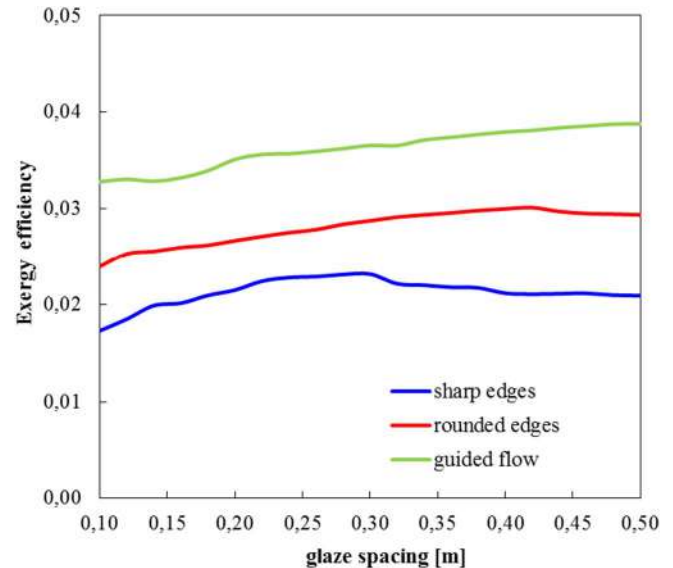


Fig. 13. Exergy efficiency per unit depth of the wall for the three configurations.

6. Conclusions

The exergy and energy performances of classic and modified Trombe-Michel Walls (TMW) are evaluated numerically by varying the thickness of the interspace between wall and glass for the three configurations of the vent investigated (“sharp edges”, “rounded edges” and with “guided flow”).

The main conclusions of the present study are the followings. The “guided flow” configuration reports the best performances, but is able to improve air flow only for narrow channels. The presence of the re-circulating zone at the bottom of the channel has a negative influence on the heat transfer, because it decreases the amount of cool air available close to the wall. The “guided flow” configuration presents small conductive heat transfer through the wall and large heat transfer in the volume, because it transfers more heat in real time, while the other two configurations transfer more heat with a time lag. The “guided flow” configuration presents the greatest exergy gain, and thermal and exergy efficiencies.

References

- [1] Directive 2010/31/eu of the European Parliament and of the Council of 19 May 2010 on the Energy Performance of Buildings, <http://www.epbd-ca.euS>, (2010).
- [2] A.R. Mansour, An approximate analytical solution to convective laminar heat transfer flow with the Trombe wall channel, *Int. Commun. Heat Mass Transfer* 18 (1991) 153–159.
- [3] B.A. Jubran, M.A. Hamdan, B. Tashtoush, A.R. Mansour, An appropriate analytical solution for the prediction of transient response of the Trombe wall, *Int. Commun. Heat Mass Transfer* 20 (1993) 567–577.
- [4] B. Zamora, J. Hernandez, Influence of variable property effects on natural convection flows in asymmetrically-heated vertical channels, *Int. Commun. Heat Mass Transfer* 24 (8) (1997) 1153–1162.
- [5] A.G. Fedorov, R. Viskanta, Turbulent natural convection heat transfer in an asymmetrically heated, vertical parallel-plate channel, *Int. J. Heat Mass Transf.* 40 (1997) 3849–3860.
- [6] G. Gan, A parametric study of Trombe walls for passive cooling of buildings, *Energy Build.* 17 (1998) 37–43.
- [7] W.N. Hien, W. Liping, A.N. Chandra, A.R. Pandey, W. Xiaolin, Effects of double glazed façade on energy consumption, thermal comfort and condensation for a typical office building in Singapore, *Energy Build.* 37 (2005) 563–572.
- [8] A. Ucar, M. Inalli, Thermal and exergy analysis of solar air collectors with passive augmentation techniques, *Int. Commun. Heat Mass Transfer* 33 (2006) 1281–1290.
- [9] B. Cheng, J. Zhao, C. Chen, Z. Zhuang, Experimental investigation of natural convection in Trombe wall systems, *Proceedings of the Sixth International Conference for Enhanced Building Operations (ICEBO 2006)*, Envelope Technologies for Building Energy Efficiency Vol. II-3-1, Shenzhen, China, 6–9 November 2006.
- [10] J. Shen, S. Lassue, L. Zalewski, D. Huang, Numerical study on thermal behavior of classical or composite Trombe solar walls, *Energy Build.* 39 (2007) 962–974.
- [11] B. Zamora, A. Kaiser, Thermal and dynamic optimization of the convective flow in Trombe Wall shaped channels by numerical investigation, *Heat Mass Transf.* 45 (2009) 1393–1407, <http://dx.doi.org/10.1007/s00231-009-0509-6>.
- [12] W. Sun, J. Ji, W. He, Influence of channel depth on the performance of solar air heaters, *Energy* 35 (2010) 4201–4207.
- [13] D. Ospir, C. Popa, C. Chereches, G. Polidori, S. Fohanno, Flow visualization of natural convection in a vertical channel with asymmetric heating, *Int. Commun. Heat Mass Transfer* 39 (2012) 486–493.
- [14] W. Pasut, M. De Carli, Evaluation of various CFD modelling strategies in predicting air flow and temperature in a naturally ventilated double skin façade, *Appl. Therm. Eng.* 37 (2012) 267–274.
- [15] M. Rabani, V. Kalantar, A.K. Faghieh, M. Rabani, R. Rabani, Numerical simulation of a Trombe wall to predict the energy storage rate and time duration of room heating during the non-sunny periods, *Heat Mass Transf.* 49 (10) (2013) 1395–1404.
- [16] A. Fudholi, K. Sopian, M.Y. Othman, M.H. Ruslan, B. Bakhtyar, Energy analysis and improvement potential of finned double-pass solar collector, *Energy Convers. Manag.* 75 (2013) 234–240.
- [17] P.M. Behbahani, R.B. Kazerouni, H. Davar, Optimization of air channel geometry on Trombe wall for transmitting excessive heat, *Indian J. Fundam. Appl. Life Sci.* 4 (S3) (2014) 877–889.
- [18] M. Lobna, D. Leila, A numerical study of heating and cooling by a Trombe wall in Tunisia, *The fifth International Renewable Energy Congress (IREC)*, 2014 (Hammamet, Tunisia).
- [19] F. Abbassi, L. Dehmani, Experimental and numerical study on thermal performance of an unvented Trombe wall associated with internal thermal fins, *Energy Build.* 105 (2015) 119–128.
- [20] W. He, Z. Hu, B. Luo, X. Hong, W. Sun, J. Ji, The thermal behavior of Trombe wall system with venetian blind: an experimental and numerical study, *Energy Build.* 104 (2015) 395–404.
- [21] W.S. Fu, W.S. Chao, T.E. Peng, C.G. Li, Flow downward penetration of vertical parallel plates natural convection with an asymmetrically heated wall, *Int. Commun. Heat Mass Transfer* 74 (2016) 55–62.
- [22] S. Chamoli, Exergy analysis of a flat plate solar collector, *J. Energy S. Afr.* 24 (3) (2013) 8–13.
- [23] P.L. Betts, I.H. Bokhari, Experiments on turbulent natural convection in an enclosed tall cavity, *Int. J. Heat Fluid Flow* 21 (6) (2000) 675–683.
- [24] F.R. Menter, Zonal two equation k- ω turbulence models for aerodynamic flows, *AIAA Paper* 93-2906, 1993.
- [25] V. Yakhot, S.A. Orszag, S. Thangam, T.B. Gatski, C.G. Speziale, Development of turbulence models for shear flows by a double expansion technique, *Phys. Fluids A* 4 (7) (1992) 1510–1520.
- [26] P.A. Durbin, Separated flow computations with the k-epsilon-v2 mode, *AIAA J.* 33 (4) (1995) 659–664.
- [27] B.E. Launder, G.J. Reece, W. Rodi, Progress in the development of a Reynolds-stress turbulent closure, *J. Fluid Mech.* 68 (3) (1975) 537–566.
- [28] M. Wolfstein, The velocity and temperature distribution of one-dimensional flow with turbulence augmentation and pressure gradient, *Int. J. Heat Mass Transf.* 12 (1969) 301–318.